Development of a high-speed ultrasonic tomography system for measurements of rising bubbles in a horizontal cross-section

Murakawa, H.; Tomoyuki, S.; Eckert, S.;

Originally published:

June 2021

Measurement 182(2021), 109654

DOI: https://doi.org/10.1016/j.measurement.2021.109654

Perma-Link to Publication Repository of HZDR:

https://www.hzdr.de/publications/Publ-32869

Development of a high-speed ultrasonic tomography system for measurements of rising bubbles in a horizontal cross-section

Abstract

The present study deals with high-speed ultrasonic tomography (UT) as a powerful tool to characterize the behavior of multiphase flows. A major goal of the work is to improve the temporal resolution for the detection of transit flow structures and time-dependent phenomena such as the incidence of rising gas bubbles. A special transducer with a wide divergence angle of 110° and a vertical height of the measurement volume of approx. 4 mm was developed and tested. The system thus enables the acquisition of cross-sectional images at a frame rate of up to 1,000 frames/s. Scatter noise was eliminated using a time series filtering method. This UT system was applied to a chain of gas bubbles rising in a cylindrical container with an internal diameter of 50 mm. The measurement system provides qualitative observations of the turbulent dynamics of bubbly flows including bubble-bubble interactions, such as the coalescence of individual bubbles.

Keywords: full-matrix capture, reflection mode, time-series filtering, pseudo three-dimensional image, bubble column, large divergence-angle transducer

1. Introduction

Two-phase flows are widely used in many industrial applications. Knowing how gas bubbles move and interact in a liquid is an extremely important prerequisite for developing suitable strategies for efficient and safe industrial processes and for achieving optimal product quality. As the bubble motion strongly depends on the shape and the size of the bubble and/or the distance between two neighboring bubbles, the evaluation of the instantaneous gas distribution, the frequency of passing bubbles and the measurement of bubble size, shape and velocity provide important and valuable information for a better understanding of the dynamics of two-phase flows. To this end, numerous studies have already been carried out on bubble movement for single bubbles and bubble plumes [1, 2]. Sanada et al. [3] reported that trajectories of bubbles released continuously at the injector depend on the detachment frequency. . The dispersion of the bubble position increases with increasing frequency, since the distance between successive bubbles decreases and the ascending bubble is influenced to a greater extent by the wake of the leading bubble. . Detailed knowledge about bubble-bubble interactions or the effects occurring in the turbulent wakes of the bubbles is important for interpreting the differences in behavior between a single bubble and bubble plumes [4].

Further investigations are required for two-phase flows particularly in opaque fluids such as

liquid metals. So far, only few data exist for this, as optical measurement methods cannot be used here due to the non-transparency. Previous experimental studies were performed [5-7] using X-ray and neutron radiographies for flow visualization. However, the size of the flow channel is limited depending on the radiation attenuation by the working fluid, hence, investigations in gallium alloys have been conducted in rectangular channels with thicknesses of less than 20 mm.

Various tomography techniques based on different physical principles, such as X-ray or neutron radiation [8, 9], electrical conductivity or capacitance [10], and ultrasonic transmission or reflection [11, 12], have been developed. Applicability, efficiency and resolution of these techniques varies depending on the properties of the fluids to be investigated. Ultrasonic techniques represent a highly effective tool in the process industry [13] as they can be applied to opaque fluids and are easy to use. The propagation of ultrasonic waves in solids and liquids are affected by reflection, diffraction, scattering, and transmission. The resulting effects can be exploited for measurement purposes. Reflection and diffraction methods rely on echo intensity detection and the time-of-flight (TOF) measurements of pulses and are applied for non-destructive testing within materials. The transmission technique is widely used in flow meters for calculating the volumetric flow rate from the TOF between

two sensors. Changes in the signal attenuation and the wave frequency are also analyzed. A suitable arrangement of a multitude of sensors combined with appropriate data evaluation is the basis of ultrasonic tomography (UT), which can be employed to obtain two-dimensional (2D) or three-dimensional (3D) information regarding the characteristic structure of two-phase flows [14, 15]. The transmission-mode tomography relies on measuring changes in the properties of transmitted ultrasonic pulses, such as the signal intensity and the TOF between the transducers placed on the circumference of the measuring domain. Rahiman et al. [16] developed a system using fan-shaped transducers and demonstrated its capability by succeeding to identify the two-phase flow regime. The basic principle of reflection-mode tomography was developed based on the amplitude-mode (A-mode) ultrasonic array technique [17, 18]. This involves the coherent summation of the echo signals received at each transducer and is generally referred to as acoustic back projection. Langener et al. [19] developed a system to measure the cross-sectional void distribution in two-phase flows using the reflection method. Thirty-two transducers with a divergence angle of 100° were set on the circumference of a pipe with an inner diameter of 53 mm. The bubble movement was successfully detected at 62.5 frames/s. Langener et al. [20] developed a ray-tracing method that enabled the evaluation of multiple scattering events, which

often produce artifacts in two-phase flow measurements.

Ultrasonic field distribution is an important parameter which has to be taken into account for ensuring satisfying results in UT measurements. Increasing the divergence angle of the transmitters increases the measuring domain. Schlaberg et al. [21] developed large divergence-angle transducers for reflection-mode applications. They designed a transducer with a divergence angle of 70° and achieved a reconstruction rate of 100 frames/s, using 36 transducers on a 100 mm pipe measurement target. The authors also developed an imaging technique using a fan-shaped beam profile [22]. Appropriate transducers for UT systems have also been investigated by Gai et al. [23]. Xu and Xu [24] developed a UT system based on both the transmission and the TOF method to monitor bubbly flows. They used six half-cylindrical transducers with a divergence angle of 180° for the pulse emission and reception, along with 36 additional rectangular transducers for pulse reception. It was shown that bubble rising motion could be detected monitored with a time resolution of 4.8 ms in a circular vessel with an inner diameter of 187 mm. The same measuring system was tested also for flow regime identification in a horizontal pipe [25]. Li et al. [26] analyzed the effect of the divergence angle of an ultrasonic transducer on the signal amplitude in transmission-mode tomography. Although the side-lobe signal amplitude is typically

not high compared to that of the main lobe, they utilized the weaker signal amplitude in the side lobe region and showed that wider divergence angles yielded better reconstructed images of the phantom outlines.

High-speed tomography is useful for obtaining 3D information on bubble movement. Cross-sectional images of the gas-liquid interfaces are reconstructed using the corresponding echo signals received at the transducers. The scanning time for the cross-sectional information determines the temporal resolution of the image. The improvement of the temporal resolution is one of the relevant topics under consideration for high-speed UT. The measuring principle consists of emitting an ultrasonic pulse from a single transducer while the resulting echo signals are received by an arrangement of multiple sensors. The pulse emission interval selected should be longer than the TOF for each sensor. Cross-sectional information is obtained by repeating pulse emission and reception at all transducers. Thus, the reduction of the number of transducers is a key parameter for improving the temporal resolution. For achieving a reconstructed image with only a small number of transducers, Li and Hoyle [27] proposed the application of spectral analysis. Yang et al. [22] showed that the divergence angle is an important parameter for reducing the number of transducers. Tan et al. [28] developed a tomography

system to measure two-phase flow using both the transmission- and reflection-mode methods. It comprises 16 ultrasonic transducers and can successfully obtain cross-sectional images at up to 625 frames/s. Rahiman et al. [29] developed a 3D reconstruction method for bubble movement. They used 32 transducers with a divergence angle of 95° and captured cross-sectional images at 59.7 frames/s. It was shown that the bubble shape and 3D interactions could be detected. However, the temporal resolution of 16.75 ms was insufficient for measuring bubble movements, causing a distinct measuring uncertainty with respect to the positions of the interface.

The objective of this study is the development of a high-speed UT system for evaluating bubble position and bubble shape of continuously released bubbles in a circular pipe. A large divergence-angle transducer with a half-cylindrical shape was developed to generate a fan-shaped beam. The measuring system was tested by studying stationary rods, moving spheres and rising bubbles in a column with an inner diameter of 50 mm. The developed system generates pseudo-3D images at very high frame rates. Shapes of the bubbles are reconstructed from the time-series data using a time-filtering method. The results presented here demonstrate the applicability of the measuring system for reconstructing the behavior of bubble chains in a horizontal cross-sectional area.

2. Experimental setup

Fig. 1 shows a schematic of the test section. The test section was made of an acrylic resin pipe with an inner diameter of 50 mm and a total height of 240 mm. The transducers were set at a vertical position that was 140 mm from the bottom. The container was filled with water up to a height of 210 mm. Argon gas was injected through a needle with an inner diameter of 1 mm. The argon flow rate was controlled using a mass flow controller (model: 1179BX52CM1BV, MKS Instruments Deutschland GmbH), covering a flow range of up to 500 sccm (standard cubic centimeter per minute, volumetric flow rate at 0 °C under 1 atm) and with an accuracy of ±1.0% (related to full scale). Eight transducers whose properties are described in the section 4 were fixed equidistantly on the circumference of the pipe every 45° using O-rings. The fan-shaped piezoelectric elements protruded approximately 3 mm from the inner wall of the container. To accurately determine the sensor position, the TOF between each pair of sensors is measured before beginning the experiments for the container filled with water. Based on the relative distance between the sensors, the sensor positions were calculated under the assumption that the sensor installation angles were accurate. Synchronized measurements were performed using a high-speed camera (model: FASTCAM-1024PCI model 100K, Photron Ltd.) along with the UT to evaluate the reconstructed results.

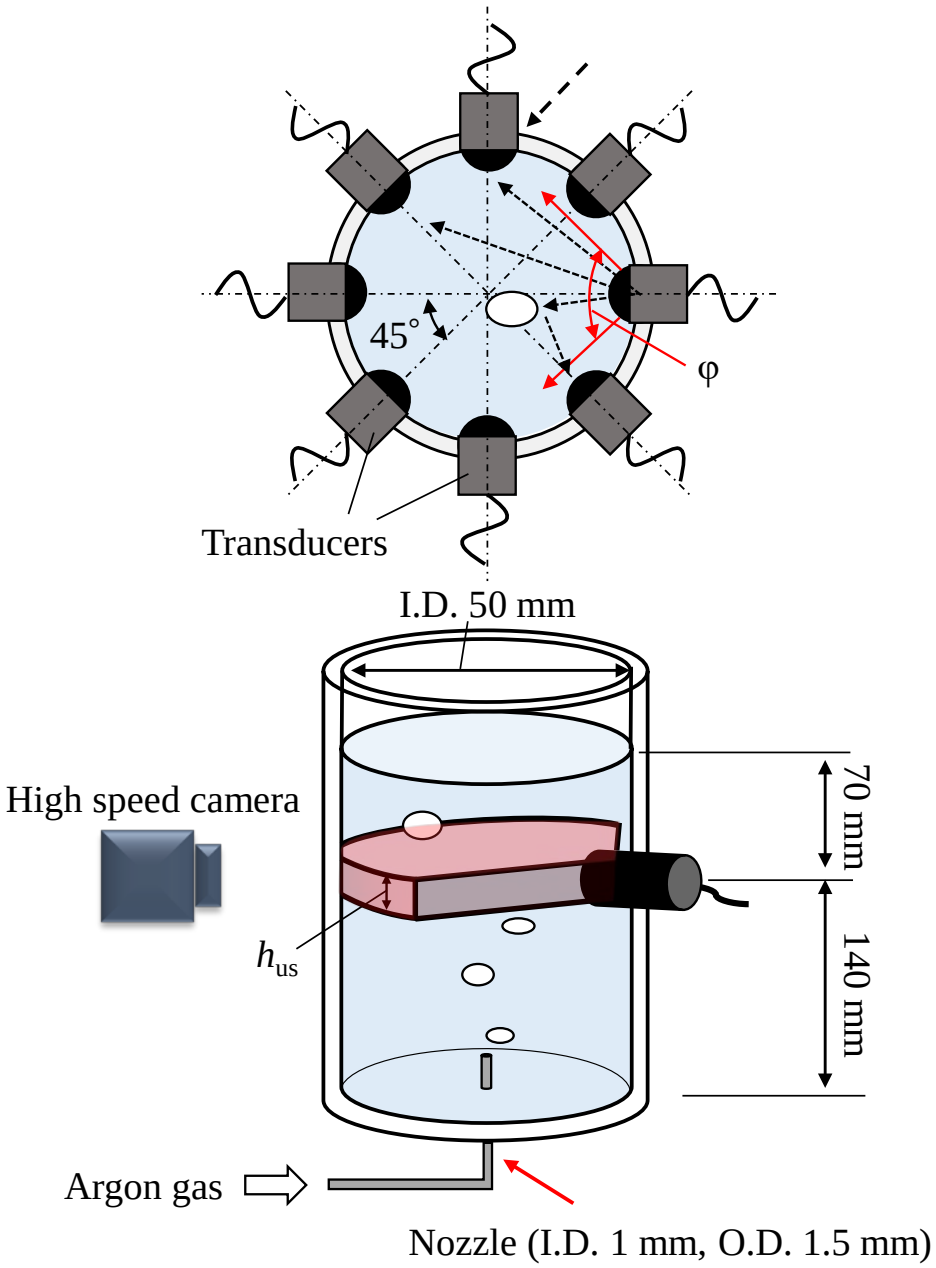

Fig. 1 Schematic representation of the test section and sensing area for reflection-mode tomography using a large divergence-angle transducer with the divergence angle φ and the lateral dimension h_{us}.

3. Selection of essential system parameters

For designing the measuring system, three important system parameters have to be considered

regarding the choice of the transducers and the related ultrasonic characteristics: the number of transducers, N_{tdx}; the ultrasonic divergence angle, φ; and the lateral dimension of the ultrasonic, h_{us} as shown in Fig. 1. In general, a larger number of sensors N_{tdx} yields a better image quality of the reconstructed two-phase flow structures in the cross-sectional image [22]. On the other hand, N_{tdx} also directly affects the temporal resolution of the measurement, Δt, as follows:

$$\Delta t = T_{\mathrm{p}} \times N_{\mathrm{tdx}} \tag{1}$$

where T_{p} is the time offset for serial actuation of the transducers. The ultrasound signal is emitted from a single transducer, and the echo signal is received at a number of transducers. The minimum T_{p} should be set taking into account the distance between the transducer and the object to be measured and the speed of sound in that medium. Δt should be as short as possible to prevent motion blur of the moving objects in the reconstructed image. From this perspective, a compromise between acceptable reconstructed image quality and optimal temporal resolution must be found when choosing N_{tdx}. Reducing N_{tdx} effectively reduces Δt, but also leads to an incomplete target outline and/or noisy cross-sectional images. A lowering of N_{tdx} can be partially compensated by a simultaneous increase of the divergence angle φ [22]. The lateral dimension of the ultrasonic beam, h_{us}, determines the measuring

volume and, hence the image resolution. It should be spatially constant to form a uniform measurement volume. If h_{us} is much larger than the target objects, it may be difficult to distinguish between individual objects at the same cross-sectional position if several objects occur simultaneously within the measurement volume. This is an essential argument for choosing a smaller value of h_{us} for reflection mode tomography. However, the application of a transducer with a small h_{us} relative to the moving distance of the target objects during Δt is problematic, since in this case the movement of the target objects to be detected within the measurement plane during the time span Δt can no longer be neglected. A suitable combination of both parameters must therefore be selected, taking into account the velocity and size of the target objects.

The value of the TOF must be at least approx. 67 μs in the pipe with an inner diameter of 50 mm, as this is the time span for a round trip of the ultrasonic pulse given a sound velocity of 1,500 m/s at 25 °C. In order to adequately take into account possible multiple reflections in the pipe, a value of the time offset T_p of more than 100 μs was specified. The typical size of the measurement targets, *i.e.*, bubbles, was of the order of several mm. For a water column at rest, bubble velocities less than 0.5 m/s can be expected. The use of 8 sensors and the choice of T_p = 125 μs results in a temporal resolution of

Δt = 1 ms. If the bubble velocity is assumed to be 0.5 m/s, the bubbles move a distance of 0.5 mm during the measurement. If h_{us} is much smaller than the bubble size, bubble detection may be difficult because the deformation of the interface can produce interfering instantaneous reflections. Therefore, h_{us} has to be of the same order of magnitude as the target size.

The detection of the liquid–gas interface position relies on the reflection of the emitted pulse at the interface which produces the echo signal which is received at the receivers. The echo signal from the bubble interface is propagating in different directions and can be obtained at the multiple transducers set on the circumference of the pipe. This information obtained at different receiving transducers is used to identify the bubble shape. Therefore, the area cross-section of the pipe covered by all of the installed transducers should be as large as possible to deliver sufficient data for the image reconstruction. Fig. 2 displays fractions of the area covered by eight transducers for different divergence angles φ. If the fraction is 1 at a position in the measurement area, ultrasonic pulses may reach the position of all transducers when there is no obstacle to the ultrasound propagation along the beam path. The figure also shows that a divergence angle of approximately 120° is appropriate for the measurement.

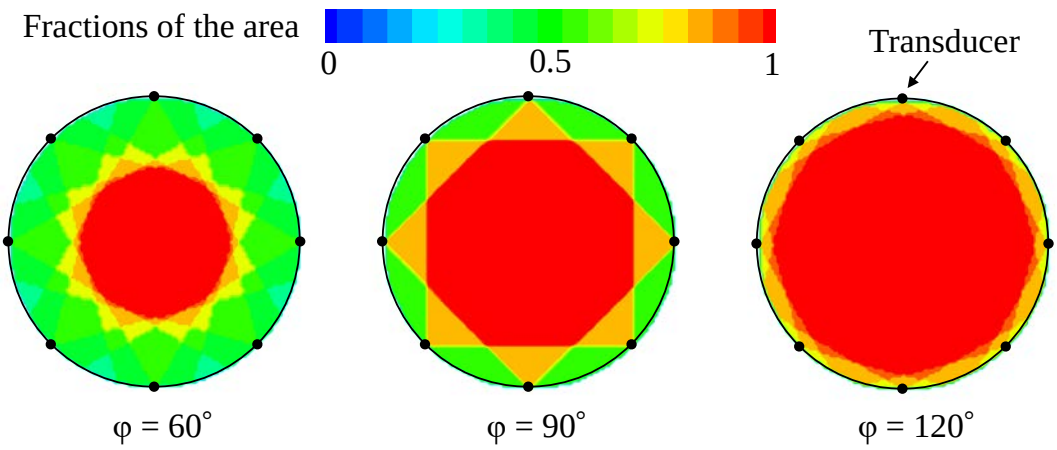

Fig. 2 Relationship between the coverage fractions of the area and the divergence angle, φ.

4. Ultrasonic transducer

Based on these considerations, a large divergence-angle ultrasonic transducer was developed, as shown in Fig. 3. The transducer contains a piezoelectric element with a circular arc. The radius and the arc angle are 5 mm and 120°, respectively. The height of the element is 5 mm and the resonant frequency f_0 is 5 MHz.

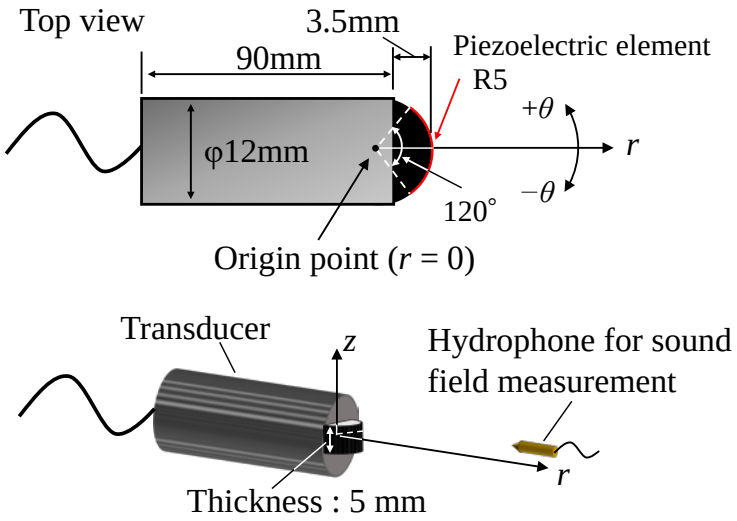

Fig. 3 Details of the large divergence-angle transducer with coordinate axes.

The ultrasound field distribution of the transducer is investigated. We use a coordinate system of the cylindrical coordinates r, θ and z which origin is set at the 5 mm behind the transducer surface, as indicated in Fig. 3. The origin point is considered as the representative position of the transducer. A needle hydrophone (model: HNC-0400, Onda Corp.) with an effective diameter of 0.4 mm was used for the pulse reception. The ultrasonic transducer and the hydrophone were set in a box filled with water. The ultrasonic transducer was connected to a pulser/receiver to emit ultrasonic pulses. The hydrophone was connected to a digitizer (NI-5114, National Instruments Corp.) to record the signal. The hydrophone was rotated around the point of origin so that the tip of the needle pointed towards the transducer. For various positions of the hydrophone, the peak-to-peak signal amplitude, V_{pp}, was obtained from the

recorded signal at each position.

Fig. 4 shows the change in the sound pressure associated with varying θ at r = 55 mm. $\bar{V}_{\mathrm{pp}}$ represents the peak-to-peak value of the sound pressure V_{pp} normalized to the maximum amplitude detected in the measurements. The profiles in Fig. 4 confirm that the sound pressure is almost constant between θ = ±55°. For values at θ = ±65°, the sound pressure decreases steeply. Fig. 5 shows the 2D sound pressure distribution at θ = 0°. The surface of the transducer is at r = 5 mm. The ultrasound pressure gradually decreases with increasing distance from the transducer. However, the sound pressure is high in a range of ±2 mm in z-direction, and no divergence and no large side-lobes of the ultrasonic field distribution are found. The results indicate that the developed transducer has an effective divergence angle of 110°, and the effective lateral dimension h_{us} is almost constant at 4 mm. It is confirmed that the large divergence-angle transducer would be suitable for use in reflection-mode tomography.

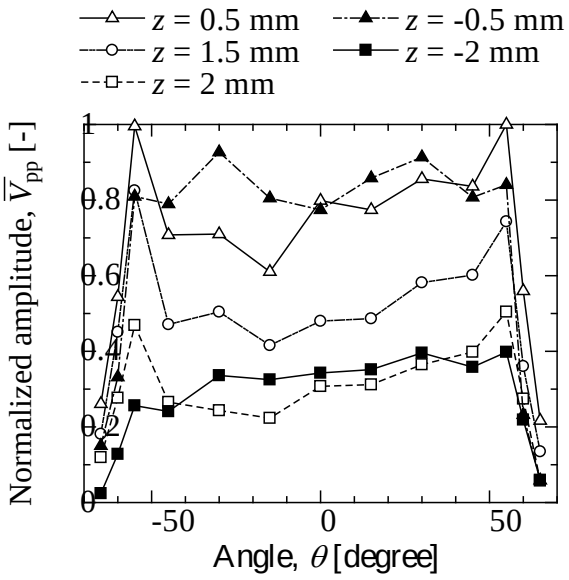

Fig. 4 Variation of normalized amplitudes of the sound pressure as a function of θ at r = 55 mm.

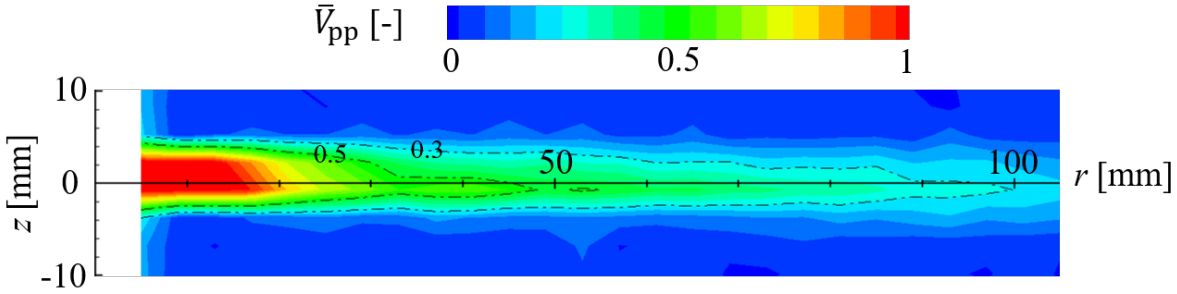

Fig. 5 Two-dimensional ultrasonic field distribution at θ = 0°.

5. Methodology

5.1 Reflection-mode tomography

This reflection-mode tomography relies on the intensity back projection of the pulse-echo signals [17]. The first transducer emits a pulse, while the echo signals are received by all the transducers,

including the transmitter. In the course of the measurement, the active role of the transmitter alternates between the transducers, switching in sequence after each pulse emission, so that ultrasonic pulses are emanated from all transducers. This technique is known as full-matrix capture [30].

The signal intensity, $V_{\mathrm{p}}(\tau)$, is calculated as the maximum amplitude of the received waveform at a transducer, $V(\tau)$, in the range $\tau \pm \frac{T_0}{2}$, where τ is the TOF of the pulses and T_0 is a period of the burst ultrasonic signals. It is necessary to remove all signals emitted by other sensors and propagating directly to the receivers, caused by multiple ultrasonic reflections in the measurement area and originating from echoes at the wall or the other sensors. To identify the echo signals from the liquid–gas interface, the difference in amplitude between the measured data and calibration data, $V_{\mathrm{p},0}$, is calculated to reduce these artifacts as follows:

$$V_{\mathrm{p,Cal}}(\tau) = V_{\mathrm{p}}(\tau) - V_{\mathrm{p},0}(\tau) \tag{2}$$

$V_{\mathrm{p},0}$ is the signal amplitude without bubble reflection, which is considered to be the base condition and is measured at the pipe filled with water. $V_{\mathrm{p,Cal}}(\tau)$ is calculated for each transmitter-*i* and receiver-*j* pair and is referred to as $V_{\mathrm{p,Cal}_{i,j}}(\tau)$.

Based on the transducer locations and the TOF, $V_{\mathrm{p,Cal}_{i,j}}(\tau)$ are linearly back-projected to

obtain the intensity distribution, $I_{i,j}(x, y)$. When a number of transducers, N_{tdx}, is used for the measurement, $N_{\mathrm{tdx}} \times N_{\mathrm{tdx}}$ echo signals are obtained. The final intensity distribution $I(x, y)$ can be expressed as follows:

$$I(x,y) = \sum_{i=1}^{N_{\mathrm{tdx}}} \sum_{j=1}^{N_{\mathrm{tdx}}} I_{i,j}(x,y) \tag{3}$$

$I(x, y)$ becomes large at positions where the reflection intensity is high, such as at the liquid–gas interface. The higher intensity appears as an elliptical arc with focal points at the transmitter and receiver positions in the cross-section. By overlapping the elliptic arcs calculated from the multiple echo signals in each transducer, the shape of the bubble interface can be recognized as the higher intensity region. The elliptic arcs appear at the bubble interface and at places where no bubbles exist. Therefore, $I(x, y)$ can include various artifacts. A weight distribution function, $F(x, y)$, is newly proposed to suppress the number of artifacts. Fig. 6 shows a schematic of the calculation procedure for $F(x, y)$. The purpose of introducing $F(x, y)$ is to eliminate the liquid-phase region from the bubble reconstruction region. If $V_{\mathrm{p,Cal}}(\tau)$ is sufficiently high, the large amplitude of the signal can be considered as originating from the liquid–gas interface. Here, $\tau_{1_{i,j}}$ is defined at the earliest τ when $V_{\mathrm{p}_{i,j}}(\tau)$ exceeds a $V_{\mathrm{p},0}(\tau) \times 1.1$. In this case, the gas phase may be present in the region where the TOF between the transmitter, gas–liquid interface and receiver is larger than $\tau_{1_{i,j}}$. Therefore, $F_{i,j}\ (x, y)$ can be expressed as follows:

$$F_{i,j}\ (x,y) = \begin{cases} 1 & \left((R_1 + R_2)/c \geq \tau_{1_{i,j}}\right) \\ 0 & (\text{otherwise}) \end{cases} \tag{4}$$

By adding $F_{i,j}(x, y)$ for all transducers, $F(x, y)$ can be obtained as follows:

$$F(x,y) = \sum_{i=1}^{N_{\mathrm{tdx}}} \sum_{j=1}^{N_{\mathrm{tdx}}} F_{i,j}(x,y) \tag{5}$$

To reduce the artifacts, a threshold, F_{th}, is applied to $F(x, y)$. If $F(x, y)$ is lower than F_{th}, 0 is substituted for $F(x, y)$. Ultimately, the cross-sectional intensity distribution $I_{\mathrm{R}}(x, y)$ can be calculated as follows:

$$I_R(x,y) = I(x,y) \times F(x,y) \tag{6}$$

The reconstructed 2D image is calculated when $I_R(x,y)$ exceeds its threshold value of $I_{R\,\mathrm{th}}$, which removes the artifacts with low signal intensities.

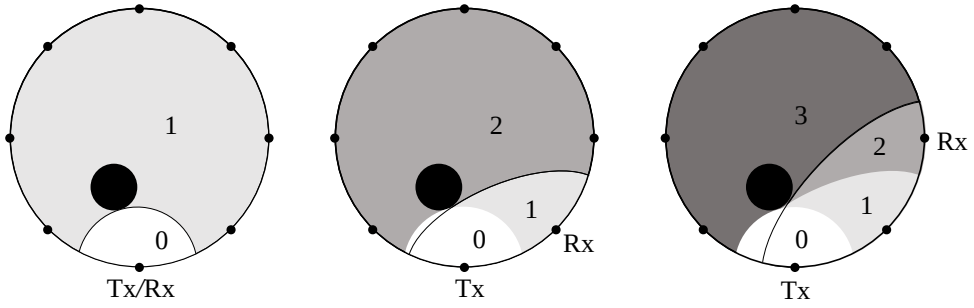

Fig. 6 Calculation of the weight distribution function, $F(x, y)$.

5.2 Design of the measuring system

A schematic of the measurement system is shown in Fig. 7. Eight transducers are used for the measurements. The ultrasonic transducers are connected to a pulser/receiver (model: JPR-10C-8CH-KB, Japan Probe Co. Ltd., Japan) containing eight channels for the emission of pulses and the reception of

signals. A digital I/O board (model: PXIe-6535, National Instruments Corporation, USA) is connected to the external triggers on each channel to control the pulse emission interval. Echo-signals are recorded using a high-speed digitizer (model: PXIe-5105, National Instruments Corporation, USA) with a sampling rate of 30 MS/s (mega-samples per second). One-cycle 5 MHz burst are emitted as the ultrasonic pulses. With this system, a full-matrix capture is possible with a minimum T_p of 5 μs.

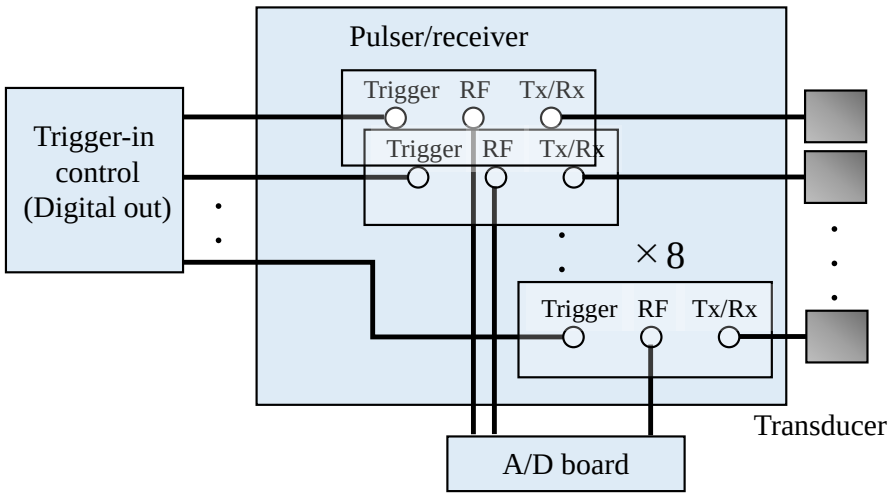

Fig. 7 Schematic of measurement system for reflection-mode tomography.

Taking the TOF and the reverberation within the measurement area in the 50 mm pipe into consideration, T_p was set to 0.125 ms, resulting in Δt = 1 ms. With increasing measurement distance, T_p should increase owing to the growing TOF. All waveforms are stored in the high-speed digitizer's on-board memory during the measurements. After the recording process has been completed, all waveforms are transferred to a PC, where the post-processing reconstruction is performed. Under these

conditions, the maximum frame rate that could be achieved for the cross-sectional image is 1,000 frames/s. The measurement interval for each cross-sectional measurement is set to 1 ms considering the bubble rising velocity and the on-board memory capacity. Therefore, 488 cross-sectional images are obtained during one measurement at 500 frames/s, which corresponds to 0.974 s for each measurement.

The experiments were carried out at room temperature (21–22 °C). The speed of sound in water is in the range of 1486–1489 m/s at this temperature. For a frequency f_0 = 5 MHz, the wavelength λ_0 is 0.30 mm in water. The measurement area of 50 × 50 mm^2 was divided into 100 × 100 sections for reconstruction resulting in a spatial resolution of 0.5 × 0.5 mm^2.

6. Results and discussion

6.1 Detection of stationary rods

To evaluate the applicability of the system and the developed algorithm, stainless-steel rods with a diameter of 6 mm were used as a phantom for reconstructing an image. The rod length was sufficiently long in comparison with h_{us}.

Fig. 8 shows the results obtained from different test cases involving one, two, and three rods. $\bar{I}(x,y)$, $\bar{F}(x,y)$, and $\bar{I_R}(x,y)$ are the respective values normalized to their corresponding maximum values. Due to the normalizations, the constant threshold values in $\bar{F}_{\mathrm{th}}$ and $\bar{I_R}_{\mathrm{th}}$ can be used for $\bar{F}_{\mathrm{th}}(x,y)$ and $\bar{I_R}_{\mathrm{th}}(x,y)$. In this case, $\bar{F}_{\mathrm{th}} = 0.9$ and $\bar{I_R}_{\mathrm{th}} = 0.2$ are determined by evaluating the reconstructed image of the rods. The black circles in Fig. 8(c) represent the real locations of the rod

surfaces. The rod locations are qualitatively derived from $\bar{I}(x,y)$. However, higher intensities are found in addition to the rod surface in $\bar{I}(x,y)$ in the cases of 2- and 3-rod. It proves impossible to obtain the rod position from $\bar{I}(x,y)$ alone, except for the single rod. As the number of rods increase, the average value of $\bar{F}(x,y)$ increases. However, $\bar{I_R}(x,y)$ can be used to reconstruct the rod locations in the 2-rod case. In the 3-rod case, artifacts appear between the rods. Because the difference in $\bar{F}(x,y)$ becomes small in terms of cross-sectional area with an increasing number of rods, artifact elimination is difficult using $\bar{F}_{\mathrm{th}}$. Because N_{tdx} is limited, the difficulty associated with the detection of a target behind other objects makes reconstruction of the image difficult. Two rods are clearly identified, whereas the detection becomes difficult in the case of three rods.

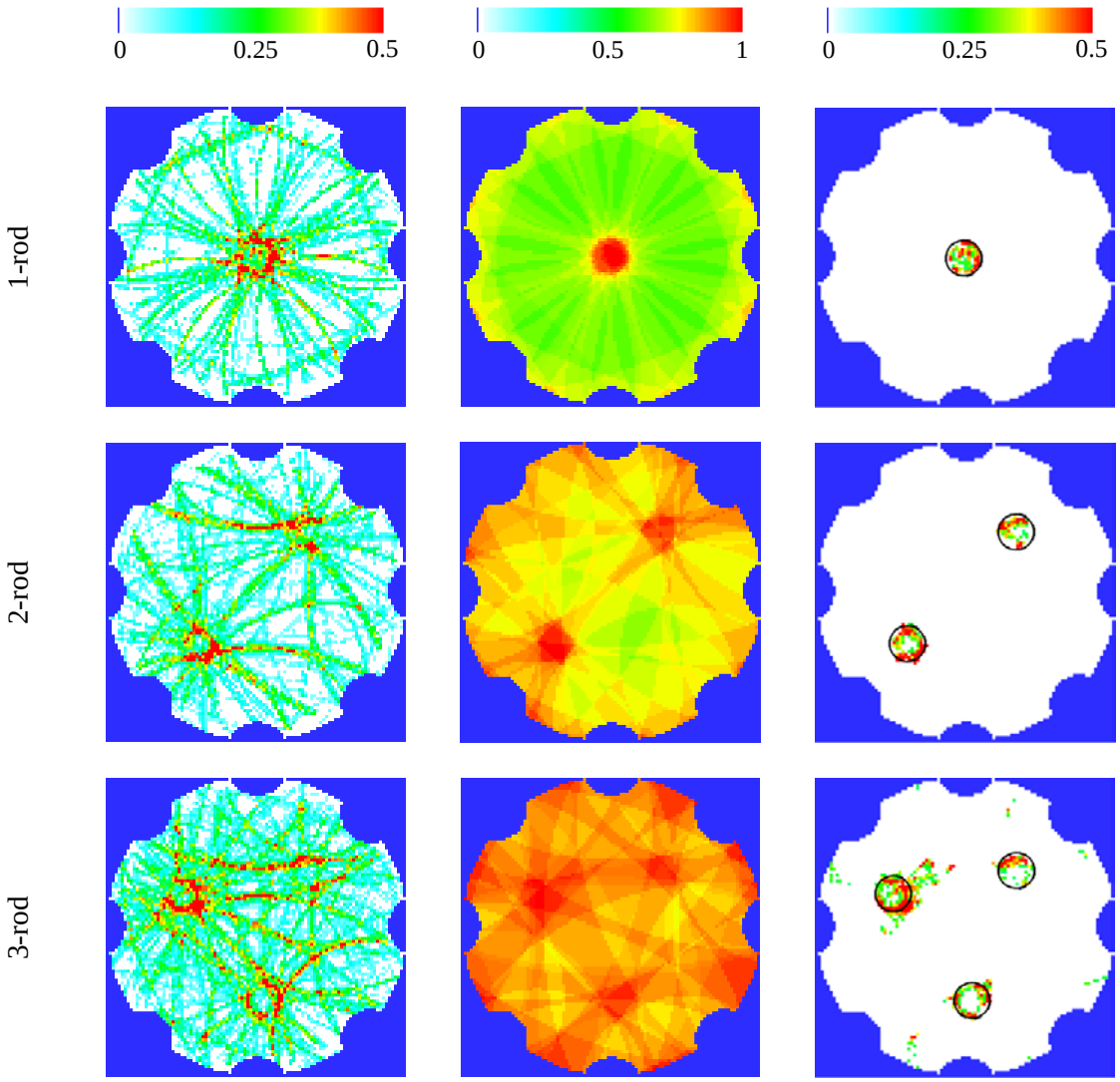

(a) $\bar{I}(x,y)$ (b) $\bar{F}(x,y)$ (c) $\bar{I_R}(x,y)$

Fig. 8 Reconstruction results of $\bar{I}(x,y)$, $\bar{F}(x,y)$ and $\bar{I_R}(x,y)$ for stationary rods.

1

2

3 6.2 Detection of moving spheres

4 Reconstruction tests were also performed using moving targets. In these experiments, a

5 stainless-steel sphere with a diameter of 6 mm was employed, along with four different sizes of acrylic

6 spheres with diameters ranging between 2.4 and 8.0 mm. Each sphere was dropped into the water from

7 the top of the container.

Fig. 9 shows the reconstructed image of the moving stainless-steel sphere. The contour represents I_R normalized to the maximum value in the time-series of the reconstructed image. Typically, the maximum intensity appears when a sphere crosses the measurement volume. Therefore, $\bar{I}_R(x, y)$ becomes small if there is no reflector in the measurement volume, which makes it easier to eliminate the artifacts using $\bar{I}_{R\mathrm{th}}$. The outer shape of the sphere is clearly confirmed. The black circle represents the estimated shape. The average diameter of the sphere calculated from the reconstructed image is 6.5 mm. Although the diameter is overestimated, the difference is almost identical to the spatial resolution. Displaying a pseudo 3D image of a continuously moving object is useful for easy recognition of the target. Here, the method used by Rahiman et al. [29] is applied. Fig. 10 shows the reconstruction of the pseudo 3D image of the stainless-steel sphere. In this experiment, the sphere's shape is identified in four consecutive frames. Because the tomography is performed at a frame rate of 500 frames/s, a tomography image can be plotted on the time axis every 2 ms. The color of the image frames is lineally interpolated. The resultant iso-intensity surface is shown in Fig. 10(b). As in the case of the stationary rods, threshold values of $\bar{F}_{\mathrm{th}} = 0.9$ and $\bar{I}_{R\mathrm{th}} = 0.2$ are used. Average dropping velocity of the sphere at the measurement position is determined to be 0.70 m/s using the high-speed camera. The time step between the four images is 6 ms. Therefore, the equivalent moving distance of the stainless-steel sphere, *i.e.* average velocity × detection time, becomes 4.2 mm. This distance is shorter than the sphere diameter of 6 mm.

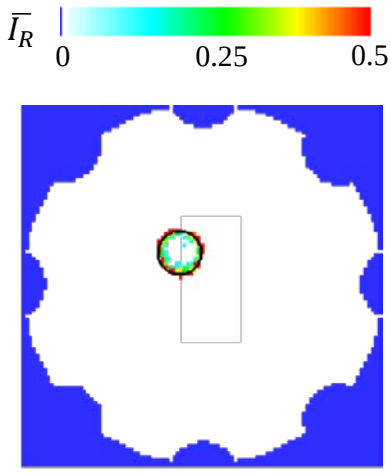

Fig. 9 A temporal reconstructed image of the moving stainless-steel sphere

1

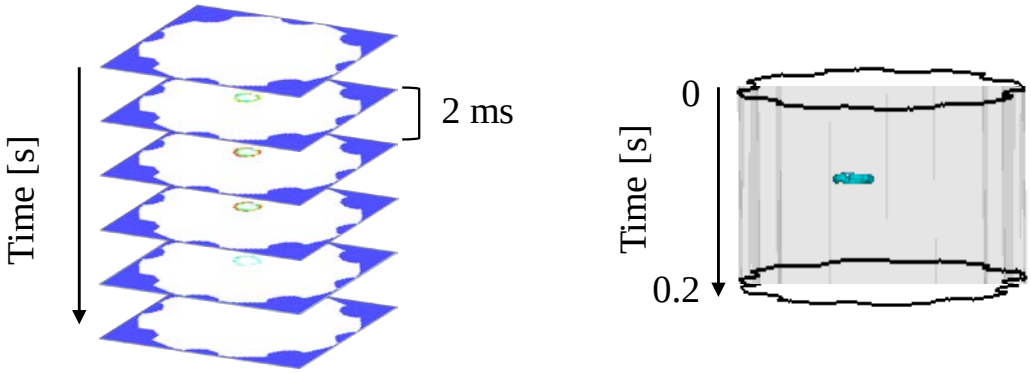

(a) 3D reconstruction (b) Iso-intensity surface

Fig. 10 Pseudo 3D image of the moving stainless-steel sphere.

2

3 Fig. 11 shows the results for the acrylic spheres of varying diameter. When only one target is
4 present in the measurement volume, the image can be correctly reconstructed for any diameter of the
5 target. However, it is difficult to confirm a complete circular outline in all the frames. This shows that
6 the interface could not be detected even though target objects are completely inside the measurement
7 volume. The pseudo 3D image results are shown in Fig. 12. Although the measurement accuracy is not
8 high in each frame, the sphere movement can clearly be reconstructed in the pseudo 3D images. The
9 average velocity measured using the high-speed camera, the detection time of the sphere calculated from

the number of reconstructed images in which the sphere appears, and the equivalent moving distance are summarized in Table 1. It is clear that the equivalent moving distance of the spherical targets is shorter than the sphere diameter. As h_{us} is approximately 4 mm as shown in Fig. 4, it appears that the high-intensity ultrasonic reflections only occur at a few points on the sphere. Because almost no ultrasonic reflection originates when a sphere enters or leave the measurement volume, it is not easy to detect the sphere's surface at these moments. Thus, it is considered that the detection time of the spheres changes with $h_{us.}$ However, the cross-sectional diameter and the position of the bubble can be detected when the bubble center is in the measurement volume.

Table 1 Relation between the acrylic sphere diameters, velocities and the detection time using the UT.

Sphere diameter	Average velocity	Detection time of the spheres	Equivalent moving distance
2.4 mm	0.051 m/s	38 ms	1.9 mm
4.0 mm	0.070 m/s	34 ms	2.4 mm
6.4 mm	0.087 m/s	30 ms	2.6 mm
7.9 mm	0.097 m/s	32 ms	3.1 mm

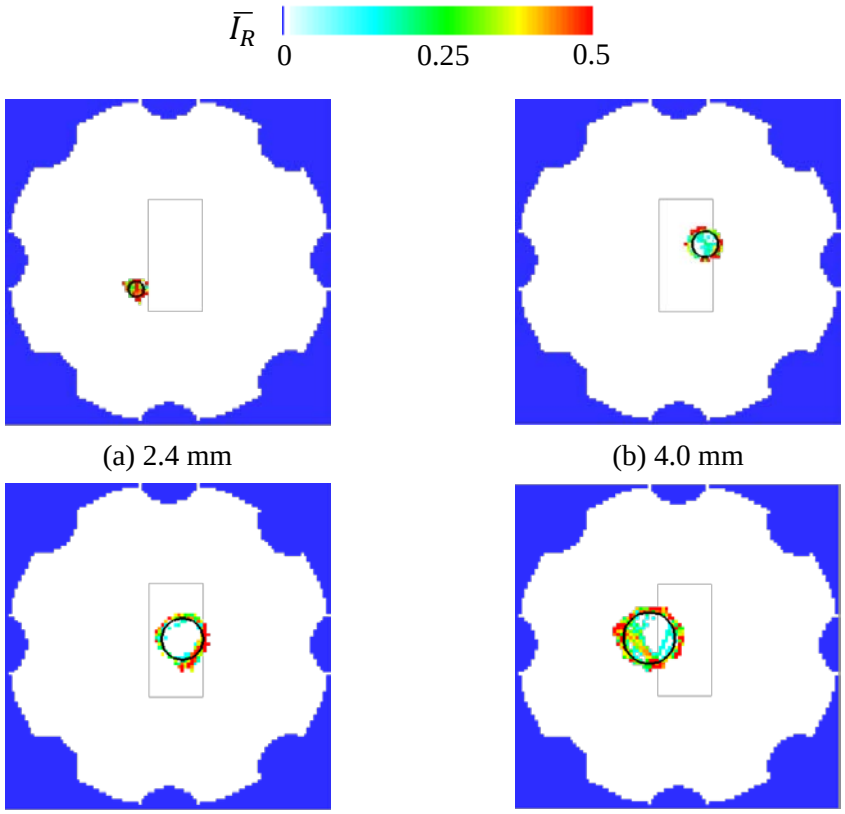

(a) 2.4 mm (b) 4.0 mm

(c) 6.4 mm (d) 7.9 mm

Fig. 11 Reconstructed images of acrylic spheres with different diameters.

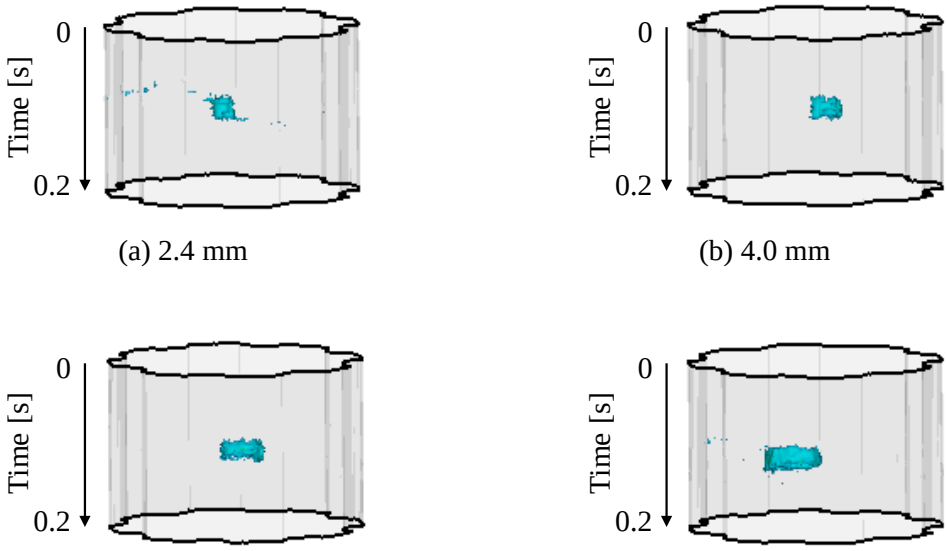

(a) 2.4 mm (b) 4.0 mm

(c) 6.4 mm (d) 7.9 mm

Fig. 12 Pseudo 3D images of acrylic spheres.

6.3 Bubble chain in a container

Argon gas was injected via the bottom nozzle at a flow rate, Q, of 15, 30, 60, and 120 sccm. Fig. 13 shows the pseudo 3D image at Q = 120 sccm between 0 and 0.974 sec. The threshold values as used so far for the stainless-steel rods and the moving spheres, $\bar{F}_{\mathrm{th}} = 0.9$ and $\bar{I_R}_{\mathrm{th}} = 0.2$, are maintained here. It can be confirmed that scattering noises are detected over the measurement period. These noises are mainly due to the liquid–gas interfaces. As the number of bubbles increases, multiple reflections between bubbles causes noise in the pseudo 3D image.

A significant reduction of the scattering noise can be achieved by optimizing the threshold values $\bar{F}_{\mathrm{th}}$ and $\bar{I_R}_{\mathrm{th}}$. A time-series filtering method is suggested to facilitate the threshold determination. Fig. 14 shows a schematic of the filtering process. Because the bubble velocity ranges between 0.2–0.3 m/s, it can be expected that the echo signals from the bubble appear in more than six continuous frames. The temporal change in $\bar{I_R}$ at a particular position is shown schematically in the Fig. 14. If a bubble moves into this domain, $\bar{I_R}$ becomes large due to the ultrasonic reflection at the interface. The average intensity, $\overline{I_{\mathrm{ave}}}$, and its standard deviation $\bar{I_\sigma}$ are calculated for each cross-sectional position (x, y) from the time-series data to detect the higher intensity of the signal. It is assumed that the number of frames, where bubbles are detected at the position (x, y), is smaller than the total number of frames. The following equation is used for $\overline{I_{\mathrm{th}}}(x, y)$ instead of using the constant value:

$$\overline{I_{\mathrm{th}}}(x, y) = \overline{I_{\mathrm{ave}}}(x, y) + 2\bar{I_\sigma}(x, y) \tag{7}$$

If $\bar{I_R}(x, y, t_0)$ is larger than $\overline{I_{\mathrm{th}}}(x, y)$, the range of t, where $\bar{I_R}(x, y, t)$ is larger than $\overline{I_{\mathrm{ave}}}(x, y)$, should

be defined by the start time t_1 and the end time t_2 ($t_1 \leq t_0 \leq t_2$). In this case, $\overline{I_R}(x, y, t)$ is considered to contain bubble associated data only in the range of $t_1 \leq t \leq t_2$, while the other data is filtered out. A sample of the time-series data at the center of the column is shown in Fig. 15(a). A three-period moving average is applied to $\overline{I_R}$. Fig. 15(b) shows the data after the filtering process. Some data points that are lower than $\overline{I_{\mathrm{th}}}$ but larger than $\overline{I_{\mathrm{ave}}}$ appear. These data are classified as scattering noise. It is also confirmed that the number of time-series data is limited when $\overline{I_R}$ is larger than $\overline{I_{\mathrm{th}}}$. Moreover, $\overline{I_R}$ gradually increases when a bubble enters the measurement volume and decreases when the bubble leaves. If the noise has been cancelled using a constant threshold value, liquid–gas interface data at lower intensity occurring when bubbles enter or leave the measurement volume can be inadvertently eliminated. However, this filtering method prevents the elimination of these data.

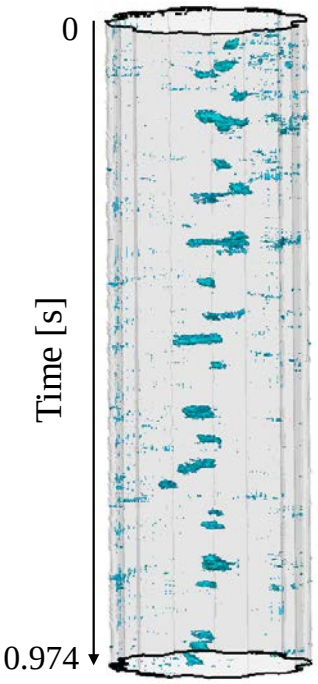

Fig. 13 Pseudo 3D image at Q = 120 sccm without the time-series filtering.

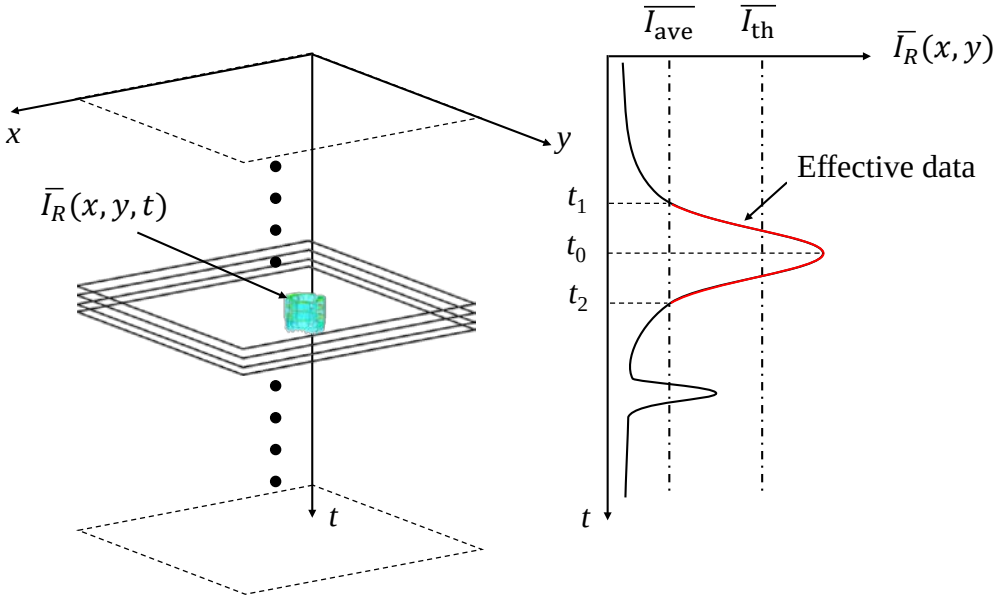

Fig. 14 Schematic of the time-series filtering.

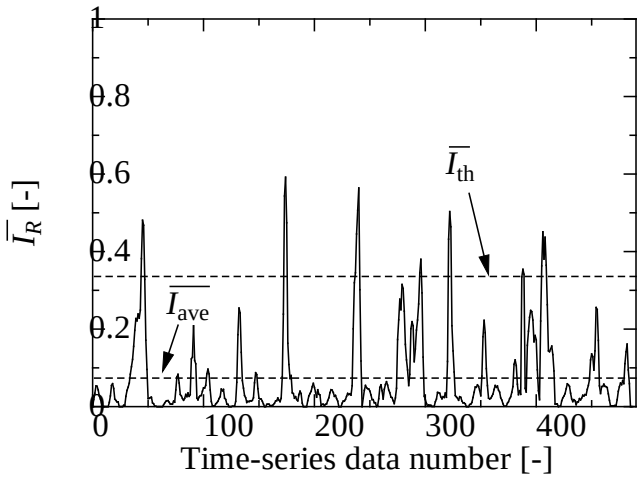

(a) Non-filtered data

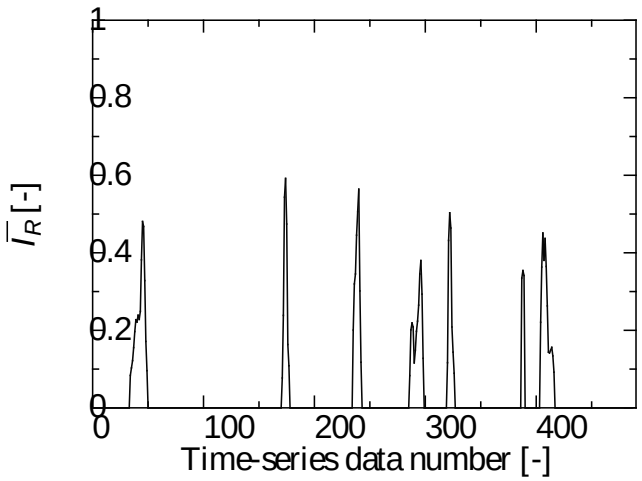

(b) Filtered data

Fig. 15 Applying the time-series filtering to $\overline{I_R}$.

Fig. 16 displays the resultant pseudo 3D images after the time-series filtering along with synchronized images obtained by the high-speed camera. The noise level is distinctly reduced, as shown for Q = 120 sccm. Since the vertical axes between the pseudo 3D image and the camera image are different, the shape of bubbles cannot be compared directly. However, it can be confirmed that the time-series filtering prevents the excessive elimination of valid bubble interface data. Because the scattering noise is not significant at low flow rates, the time-series filtering is effective particularly for higher flow

rate conditions, *i.e.*, 60 and 120 sccm. The frequency of bubble detachment from the injection nozzle was confirmed to be almost constant at Q = 15–120 sccm from the visual observation. Based on the number of bubbles and the flow rate, the volume equivalent bubble diameter is found to be 4.3–4.5 mm under these conditions.

Due to the limited number of transducers, it is difficult to completely reconstruct the outlines of bubbles in all frames. However, the high frame rate of the UT enables the reconstruction of pseudo 3D images providing valuable information about the bubble motion which also allows for a qualitative assessment of the bubble distribution in the cross-section. A comparison of the results from the UT and synchronized images obtained by the high-speed camera demonstrates that the UT can detect continuously rising bubble movements, such as for Q = 15 and 30 sccm. Further information regarding the direction of bubble movement or bubble deformation can also be obtained. Owing to the higher frame rate and the smaller h_{us}, bubble shape and movement can be clearly determined by UT from the 3D images, even if the shape of the liquid–gas interface changes over time. The distances between the bubbles become smaller for higher gas flow rates. The images obtained at 120 sccm reveal many situations where some bubbles come close to each other. When two or three bubbles are present in the measurement volume, the number of artifacts and the noise level increase. However, the bubble position and distribution in the cross-section can be qualitatively obtained.

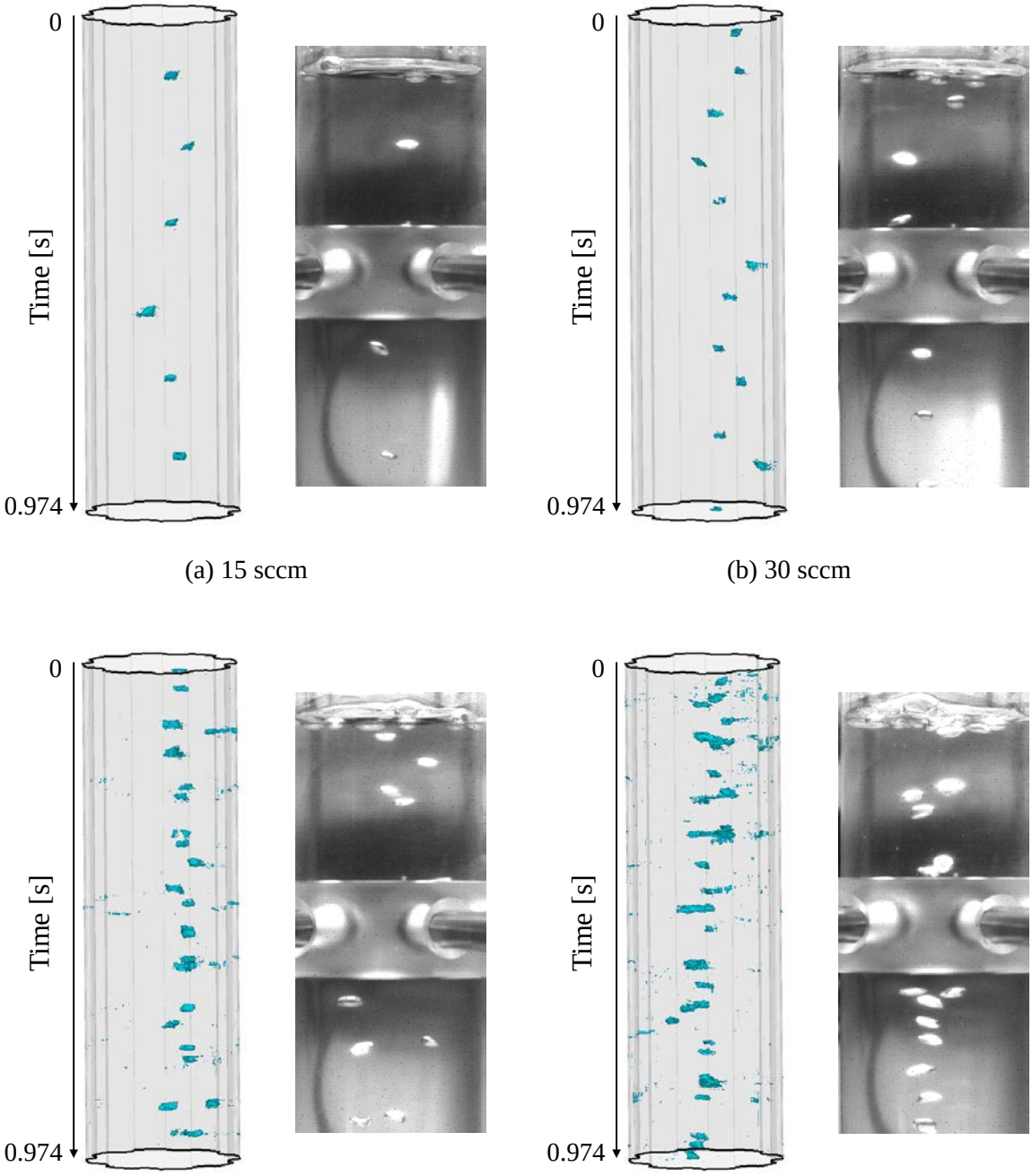

(a) 15 sccm (b) 30 sccm

(d) 60 sccm (e) 120 sccm

Fig. 16 Pseudo 3D image from UT measurements of a bubble column

7. Conclusions

A new UT system was proposed for detecting and studying the motion of bubble chains in a liquid. An ultrasonic transducer with a large divergence angle of 110° and vertical height of measuring

volume of approximately 4 mm was developed for use in reflection-mode tomography. Ultrasonic back-projection was used for the reconstruction of bubble shapes. In addition, the weight distribution function was applied to eliminate the artifacts caused by the liquid–gas interface. Furthermore, a time-series filtering method was shown to be appropriate to eliminate scattering noise in the tomography data. The UT system includes eight transducers to measure the two-phase flow in a container with an inner diameter of 50 mm. Because the pulse transmission interval is set to 0.125 μs, a temporal resolution of 1 ms is achieved. The system can detect cross-sectional images at frame rates up to 1,000 frames/s. A sphere moving at 0.7 m/s was successfully detected at 500 frames/s. The use of a restricted number of transducers limits the accuracy of the reconstructed cross-sectional images. However, the location of the bubbles can be qualitatively obtained from the pseudo 3D image. If more than 3 bubbles are located within the measurement volume, it is difficult to distinguish the bubbles and follow their outlines clearly. However, the system is capable for qualitative observations, such as motion of bubble chains and deformation of the bubble interface.

Because the velocity information is not included in the pseudo 3D image, there is no information about the bubble height. However, if the UT measurements are performed simultaneously on two planes with a small intervening distance between them, the velocity information can be obtained by analyzing the time offset in the cross-sectional images between both planes. Furthermore, UT can be used to evaluate bubble coalescence and bubble interaction if the inlet conditions are known.

Acknowledgements

The authors wish to express gratitude to Dr. D. Räbiger (HZDR) for supporting the experiments. The two-dimensional ultrasound pressure field was kindly measured by Prof. Kikura and his laboratory team (Tokyo Institute of Technology). This work was supported by JSPS KAKENHI Grant Numbers JP17H03175, JP17KK0115.

References

[1] C. Brücker, Structure and dynamics of the wake of bubbles and its relevance for bubble interaction, Physics of Fluids 11 (1999) 1781–1796. https://doi.org/10.1063/1.870043

[2] A.A. Kulkarni, J.B. Joshi, Bubble formation and bubble rise velocity in gas-liquid systems: A review, Ind. Eng. Chem. Res. 44 (2005), 5873–5931. https://doi.org/10.1021/ie049131p

[3] T. Sanada, M. Watanabe, T. Fukano, A. Kariyasaki, Behavior of a single coherent gas bubble chain and surrounding liquid jet flow structure, Chemical Engineering Science 60 (2005) 4886–4900. https://doi.org/10.1016/j.ces.2005.04.010

[4] B. Wang, S.A. Socolofsky, On the bubble rise velocity of a continually released bubble chain in still water and with crossflow, Physics of Fluids 27 (2015) 103301. https://doi.org/10.1063/1.4932176

[5] L. Liu, O. Keplinger, T. Ziegenhein, N. Shevchenko, S. Eckert, H. Yan, D. Lucas, Euler–Euler modeling and X-ray measurement of oscillating bubble chain in liquid metals, International Journal of Multiphase Flow 110 (2019) 218–237. https://doi.org/10.1016/j.ijmultiphaseflow.2018.09.011

[6] O. Keplinger, N. Shevchenko, S. Eckert, Experimental investigations of bubble chains in a liquid

metal under the influence of a horizontal magnetic field, International Journal of Multiphase Flow 121 (2019) 103111. https://doi.org/10.1016/j.ijmultiphaseflow.2019.103111

[7] T. Richter , O. Keplinger, N. Shevchenko, T. Wondrak, K. Eckert, S. Eckert, S. Odenbach, Single bubble rise in GaInSn in a horizontal magnetic field, International Journal of Multiphase Flow 104 (2018) 32–41. https://doi.org/10.1016/j.ijmultiphaseflow.2018.03.012

[8] G.D. Harvel, K. Hori, K. Kawanishi, J.S. Chang, Cross-sectional void fraction distribution measurements in a vertical annulus two-phase flow by high speed X-ray computed tomography and real-time neutron radiography techniques, Flow Measurement and Instrumentation 10 (1999) 259–266. https://doi.org/10.1016/S0955-5986(99)00008-4

[9] Y. Saito, K. Mishima, Y. Tobita, T. Suzuki, M. Matsubayashi, Measurements of liquid–metal two-phase flow by using neutron radiography and electrical conductivity probe, Experimental Thermal and Fluid Science 29 (2005) 323–330. https://doi.org/10.1016/j.expthermflusci.2004.05.009

[10] R. Banasiak, R. Wajman, T. Jaworski, P. Fiderek, H. Fidos, J. Nowakowski, D. Sankowski, Study on two-phase flow regime visualization and identification using 3D electrical capacitance tomography and fuzzy-logic classification, International Journal of Multiphase Flow 58 (2014) 1–14. http://dx.doi.org/10.1016/j.ijmultiphaseflow.2013.07.003

[11] N. Reinecke, G. Petritsch, D. Schmitz, D. Mewes, Tomographic measurement techniques – Visualization of multiphase flows, Chemical Engineering Technology 21 (1998) 7–18. https://doi.org/10.1002/(SICI)1521-4125(199801)21:1<7::AID-CEAT7>3.0.CO;2-K

[12] Y.A. Wahaba, R.A. Rahim, M.H.F. Rahiman, S.R. Aw, F.R.M. Yunus, C.L. Goh, H.A. Rahim, L.P. Ling, Non-invasive process tomography in chemical mixtures – A review, Sensors and Actuators B: Chemical 210 (2015) 602–617. https://doi.org/10.1016/j.snb.2014.12.103

[13] P. Hauptmann, N. Hoppe and A. Püttmer, Application of ultrasonic sensors in the process industry,

Application of ultrasonic sensors in the process industry, Measurement Science and Technology 13 (2002) R73–R83. https://doi.org/10.1088/0957-0233/13/8/201

[14] C.L. Goh, A.R. Ruzairi, F.R. Hafiz, Z.C. Tee, Ultrasonic tomography system for flow monitoring: A Review, IEEE Sensors Journal 17 (2017) 5382–5390. https://doi.org/10.1109/JSEN.2017.2725911

[15] M.H.F. Rahiman, R.A. Rahim, H.A. Rahim, E.J. Mohamad, Z. Zakaria, S.Z.M. Muji, An investigation on chemical bubble column using ultrasonic tomography for imaging of gas profiles, Sensors and Actuators B: Chemical 202 (2014) 46–52. https://doi.org/10.1016/j.snb.2014.05.043

[16] M.H.F. Rahiman, R.A. Rahim, M.H.F. Rahiman, M. Tajjudin, Ultrasonic transmission-mode tomography imaging for liquid/gas two-phase flow, IEEE Sensors Journal 6 (2006) 1706–1715. https://doi.org/10.1109/JSEN.2006.884549

[17] S.J. Norton, M. Linzer, Ultrasonic reflectivity tomography: Reconstruction with circular transducer array, Ultrasonic Imaging 1 (1979) 154–184. https://doi.org/10.1016/0161-7346(79)90014-2

[18] F. Wiegand, B.S. Hoyle, Simulations for parallel processing of ultrasound reflection-mode tomography with applications to two-phase flow measurement, IEEE Transactions on Ultrasonics, Ferroelectrics, and Frequency Control 36 (1989) 652–660. https://doi.org/ 10.1109/58.39116

[19] S. Langener, M. Vogt, H. Ermert, T. Musch, A real-time ultrasound process tomography system using a reflection-mode reconstruction technique, Flow Measurement and Instrumentation 53 (2017) 107–115. https://doi.org/10.1016/j.flowmeasinst.2016.05.001

[20] S. Langener, T. Musch, H. Ermert, M. Vogt, Simulation of full-angle ultrasound process tomography with two-phase media using a ray-tracing technique, 2014 IEEE International Ultrasonics Symposium (2014), 57–60. https://doi.org/10.1109/ULTSYM.2014.0015

[21] H.I. Schlaberg, M. Yang, B.S. Hoyle, M.S. Beck, C. Lenn, Wide-angle transducers for real-time ultrasonic process tomography imaging applications, Ultrasonics 35 (1997), 213–221.

https://doi.org/10.1016/S0041-624X(97)00002-4

[22] M. Yang, H.I. Schlaberg, B.S. Hoyle, M.S. Beck, C. Lenn, Real-time ultrasound process tomography for two-phase flow imaging using a reduced number of transducers, IEEE Transactions of Ultrasonics, Ferroelectrics, and Frequency Control 46 (1999), 492–501. https://doi.org/10.1109/58.764834

[23] H. Gai, MS. Beck, R.S. Flemons, An integral ultrasound transducer/pipe structure for flow imaging, Proc. of IEEE Ultrasonics Symposium (1989), 1077–1082. https://doi.org/10.1109/ULTSYM.1989.67155

[24] L.J. Xu, L.A. Xu, Ultrasound tomography system used for monitoring bubbly gas/liquid two-phase flow, IEEE Transactions of Ultrasonics, Ferroelectrics, and Frequency Control 44 (1997), 67–76. https://doi.org/ 10.1109/58.585193

[25] L.J. Xu, L. A. Xu, Gas/liquid two-phase flow regime identification by ultrasonic tomography, Flow Measurement and Instrumentation 8 (1997), 145–155. https://doi.org/10.1016/S0955-5986(98)00002-8

[26] N. Li, M. Cao, K. Xu, J. Jia, H. Du, Ultrasonic transmission tomography sensor design for bubble identification in gas-liquid bubble column reactors, Sensors 18 (2018), 4256. https://doi.org/10.3390/s18124256

[27] W. Li, B.S. Hoyle, Ultrasonic process tomography using multiple active sensors for maximum real-time performance, Chemical Engineering Science 52 (1997) 2161–2170. https://doi.org/10.1016/S0009-2509(97)00042-0

[28] C. Tan, X. Li, H. Li, F. Dong, An ultrasonic transmission/reflection tomography system for industrial multiphase flow imaging, IEEE Transactions on Industrial Electronics 66 (2019), 9539–9548. https://doi.org/10.1109/TIE.2019.2891455

[29] M.H.F. Rahiman, R.A. Rahim, H.A. Rahim, R.G. Green, Z. Zakaria, E.J. Mohamad, S.Z.M. Muji,

1 An evaluation of single plane ultrasonic tomography sensor to reconstruct three-dimensional profiles in
2 chemical bubble column, Sensors and Actuators A: Physical 246 (2016) 18–27.
3 https://doi.org/10.1016/j.sna.2016.04.058

4 [30] M. Sutcliffe, M. Weston, B. Dutton, P. Charlton, K. Donne, Real-time full matrix capture for
5 ultrasonic non-destructive testing with acceleration of post-processing through graphic hardware, NDT
6 & E International 51 (2012) 16–23. https://doi.org/10.1016/j.ndteint.2012.06.005